

Stochastic analysis of finite-temperature effects on cosmological parameters

Armin Hatefi^{*1}, Ehsan Hatefi^{†2,3}, and I. Y. Park^{‡4}

¹Department of Mathematics and Statistics, Memorial University of Newfoundland, St. John's, NL, Canada.

²University of Alcala, Department of Signal Theory and Communications, Madrid, Spain

³Scuola Normale Superiore and I.N.F.N, Piazza dei Cavalieri 7, 56126, Pisa, Italy

⁴Department of Applied Mathematics, Philander Smith University, Little Rock, AR 72202, USA.

Abstract

We explore the impact of finite-temperature quantum gravity effects on cosmological parameters, particularly the cosmological constant Λ , by incorporating temperature-dependent quantum corrections into the Hubble parameter. For that purpose, we modify the Cosmic Linear Anisotropy Solving System. We introduce new density parameters, Ω_{Λ_2} and Ω_{Λ_3} , arising from finite-temperature quantum gravity contributions, and analyze their influence on the cosmic microwave background power spectrum using advanced machine learning techniques, including artificial neural networks and stochastic optimization. Our results reveal that Ω_{Λ_2} assumes a negative value, consistent with dimensional regularization in renormalization and that the presence of Ω_{Λ_2} as well as Ω_{Λ_3} enhances model accuracy. Numerical analyses demonstrate that the inclusion of these parameters improves the fit to 2018 Planck data. Although further work is required, our results suggest that finite-temperature quantum gravity effects may play a non-negligible role in cosmological evolution. Although the Hubble tension persists, our findings highlight the potential of quantum gravitational corrections in refining cosmological models and motivate further investigation into higher-order thermal effects and polarization data constraints.

*ahatefi@mun.ca

†ehsanhatefi@gmail.com

‡inyongpark05@gmail.com

1 Introduction

The cosmological constant problem remains one of the most profound challenges in theoretical cosmology (see [1–3] for reviews and recent developments), with the observed value of vacuum energy being many orders of magnitude smaller than quantum field theory predictions. Recent works [4–6] employing finite-temperature quantum field theory (finite-T QFT) (see [7–9] for reviews) suggest that temperature-dependent quantum corrections may provide new insights into this longstanding puzzle.¹ These effects, particularly in the context of quantum gravity (QG), introduce perturbative corrections to the cosmological constant that could significantly impact our understanding of early Universe physics.

In conventional cosmology (see [11, 12] for reviews), temperature effects are typically treated through classical thermodynamics, while quantum contributions are disregarded. However, as demonstrated in [4, 5], where it was proposed that the cosmological constant (CC) problem may be a consequence of how perturbation theory and finite renormalization are handled (see [1, 2], [13], and [14] for related discussions), finite-T QFT effects naturally lead to a time-dependent cosmological constant in FLRW cosmology through loop-generated corrections. This arises from the temperature dependence of the one-particle irreducible (1PI) effective action, where the quantum-corrected cosmological constant takes the form $\Lambda_{tot} = \Lambda_1 + \Lambda_2 a^{-4} + \Lambda_3 a^{-2} + \dots$ with a the scale factor, introducing new density parameters Ω_{Λ_2} and Ω_{Λ_3} beyond the standard Ω_{Λ_1} .

Continuing the effort initiated in [15], this work presents an intensive investigation of these finite-temperature QG effects on the cosmological parameters by conducting the following tasks: firstly, we modify the Cosmic Linear Anisotropy Solving System (CLASS) Boltzmann code [16, 17] to incorporate temperature-dependent corrections to the Hubble parameter, including the new QG-induced parameters Ω_{Λ_2} and Ω_{Λ_3} . Secondly, we carry out an extensive numerical analysis by using both brute-force parameter scans and advanced machine learning techniques to constrain these parameters against the 2018 Planck data [18]. Thirdly, we develop artificial neural network (ANN) methods to efficiently explore the high-dimensional parameter space and identify optimal cosmological configurations. Studies employing ANNs to investigate cosmological parameters include [19–23].

The inclusion of finite-T QG effects addresses several key theoretical questions. First, the negative sign that emerges for Ω_{Λ_2} in our analysis finds natural explanation through dimensional regularization in the renormalization procedure. Second, while these effects are small in the present era, they become significant during the radiation-dominated epoch and near recombination, potentially influencing the interpretation of early dark energy [24]. Third, our phenomenological approach provides a framework to test whether quantum gravitational corrections could alleviate persistent tensions like the Hubble tension [25].

Our methodology combines first-principle theoretical considerations with state-of-the-art computational techniques. The modified CLASS implementation [26] allows us to systematically study how finite-T corrections affect the CMB power spectrum, while our machine

¹The central idea in [4, 5] is the introduction of a novel renormalization scheme in which the renormalized masses are chosen to be of the order of the temperature. Similar approaches were adopted in earlier works, such as [10], where problematic m^4 terms were eliminated through an alternative renormalization prescription.

learning (ML) approach enables efficient exploration of the eight-dimensional parameter space $(\Omega_{\Lambda_2}, \Omega_{\Lambda_3}, h, \omega_b, \omega_{cdm}, A_s, n_s, \tau_{reio})$.

The paper is organized as follows. Section 2 describes our modifications to CLASS. A natural question arises: given their similar scaling behaviors, could Ω_{Λ_2} and Ω_{Λ_3} be absorbed into existing parameters such as the radiation density Ω_r and the curvature density Ω_K , respectively? We address this question. Section 3 outlines our numerical methods and results, including parameter estimation using artificial neural networks (ANNs). Our approach, which is a model-building exercise, differs from the standard Bayesian parameter inference, adopting a frequentist framework augmented by machine learning techniques; the rationale behind this choice is also discussed. It is noteworthy that both the results obtained in Table 3 and Fig. 7 indicate that Ω_{Λ_2} and Ω_{Λ_3} play a crucial role in determining the fine structure of the curve. In section 4, we conclude with a discussion of the implications for cosmological models and potential future directions. In Appendix A, the non-degeneracy of Ω_{Λ_3} and Ω_K is explicitly demonstrated. Appendix B presents the ANN-based statistical method employed in the main analysis of section 3.

2 Computational framework

In this section, we outline the main computational tool developed and employed in this study to incorporate finite-T effects and analyze their cosmological implications, a modified version of CLASS Boltzmann code. We describe the modifications made to the CLASS to account for finite-temperature quantum gravitational corrections, which manifest as shifts in cosmological parameters, most notably the cosmological constant. These modifications enable the computation of power spectra under the influence of temperature-dependent vacuum energy contributions.

2.1 Conceptual framework

Before delving into the specific computational tools used in this work, it is useful to outline a more conceptual framework that motivates our overall approach. At a fundamental level, the starting point would be the action describing the Standard Model (SM) fields coupled to gravity. To this, one may append the action of an additional macroscopic system, such as a hydrodynamic fluid, which serves to model the large-scale structure and thermodynamic evolution of the Universe. Given that quantum effects are expected to play a significant role - particularly in the early Universe - it is natural to consider the 1PI effective action for the entire coupled system. More specifically, one can take the classical action of the form

$$S = S_{EH} + S_{SM} + S_{PF} \tag{1}$$

where S_{EH} denotes an Einstein-Hilbert action with a cosmological constant, S_{SM} the SM action (in a curved background), and S_{PF} a hydrodynamic or kinetic theory matter system,



Figure 1: vacuum diagrams in the pure gravity sector: (a) graviton loop (b) ghost loop

say, a perfect fluid, to be specific:

$$\begin{aligned}
\mathcal{L}_{EH} &= \frac{1}{\kappa^2} (R - 2\Lambda) \\
\mathcal{L}_{SM} &= \mathcal{L}_{gauge+gh} + \mathcal{L}_{fer} + \mathcal{L}_{Yukawa} + \mathcal{L}_{Higgs} \\
&= -\frac{1}{4} W_{\mu\nu}^i W^{\mu\nu i} - \frac{1}{4} B_{\mu\nu} B^{\mu\nu} - \partial_\mu c_a^* (\partial^\mu c_a - g f_{abc} W_c^\mu c_b) \\
&\quad - \sum_m^F \left(\bar{q}_{mL} \not{D} q_{mL} + \bar{l}_{mL} \not{D} l_{mL} + \bar{u}_{mR} \not{D} u_{mR} + \bar{d}_{mR} \not{D} d_{mR} + \bar{e}_{mR} \not{D} e_{mR} + \bar{\nu}_{mR} \not{D} \nu_{mR} \right) \\
&\quad - Y_{mn}^d \bar{q}_L^m \Phi d_R^n - Y_{mn}^u \bar{q}_L^m \tilde{\mathcal{F}} u_R^n + h.c. + (\text{leptonic sector Yukawa terms}) \\
&\quad - (D_\mu \Phi)^\dagger (D^\mu \Phi) - \frac{\lambda}{6} \left(\Phi^2 - \frac{3}{\lambda} \tilde{\mu}^2 \right)^2
\end{aligned} \tag{2}$$

where the contractions of the spacetime indices are done with the curved metric; the covariant derivatives contain both the Christoffel and gauge connections. The detailed forms and field contents of each line above as well as the overall conventions can be found in [6]. The explicit form of the action S_{PF} in the hydrodynamic matter case can be found, e.g., in [27]. One can quantize the system [6], and obtain the 1PI action. For cosmological applications, the important terms will be the classical part (or renormalized part, more precisely) and leading terms in the derivative expansion, as higher-order contributions are typically suppressed. More precisely, one can focus on the renormalized action with the coupling constants shifted by quantum effects.²

Especially, non-derivative quantum corrections, such as those contributing to the cosmological constant, can have a non-negligible impact despite their small magnitude. This is so because the observed value of the cosmological constant is itself extremely small, making even suppressed quantum effects potentially significant. Similar roles for non-derivative quantum corrections have been explored in other contexts, such as black hole accretion physics [28], underscoring their physical relevance in some situations. Shifts in the cosmological constant arise from the vacuum-to-vacuum diagrams. Fig. 1 shows the relevant diagrams in the pure

²As a slightly different and conceptually simpler approach - yet one that ultimately leads to the same starting point at the level of approximation currently adopted for cosmological studies as just described - one may employ the following setup. In this approach, one first constructs an effective field theory action without incorporating the kinetic theory component. The term "effective" can carry different meanings in the literature; here, it refers specifically to an effective field theory obtained by retaining only the leading terms in the derivative expansion of the 1PI action. Notably, quantum corrections to the cosmological constant are included. The kinetic theory system can then be coupled to this resulting field-theoretic system.

gravity sector (analogous diagrams exist in the matter-coupled sector). For example, the graviton vacuum-to-vacuum amplitude is given by:

$$\int \prod_x dh_{\kappa_1 \kappa_2} e^{\frac{i}{\kappa^2} \int \sqrt{-g} \left(-\frac{1}{2} \tilde{\nabla}_\gamma h^{\alpha\beta} \tilde{\nabla}^\gamma h_{\alpha\beta} \right)}. \quad (3)$$

Evaluation of such diagrams including the ones coming from the SM sector in a finite temperature, an example of which is given below, generically leads to the form of the CC given in the introduction [4–6]. For relevance of dynamic vacuum in the context of the CC problem, see [29, 30]

To avoid unnecessary complications associated with gravity quantization, for the moment let us consider a scalar system to illustrate one-loop generation of the CC. In a flat background:

$$S_{ren} = - \int d^4x \left[\frac{1}{2} \partial_\mu \phi \partial^\mu \phi + \frac{1}{2} m^2 \phi^2 + \frac{1}{4!} \lambda \phi^4 \right]. \quad (4)$$

where 'ren' denotes 'renormalized'. Define

$$V_{ren} \equiv \frac{1}{2} m^2 \phi^2 + \frac{1}{4!} \lambda \phi^4, \quad m_\phi \equiv m^2 + \frac{1}{2} \phi^2. \quad (5)$$

The one-loop effective potential at finite temperature is given by (see e.g., [31], the work well-known in the finite-T literature, as well as [9])

$$V_{one-loop} = V_{ren} + J(m_\phi, T) \quad (6)$$

$$\begin{aligned} J(m_\phi, T) &\equiv \oint \frac{1}{2} \ln(K^2 + m_\phi^2) = -\frac{\pi^2}{90} T^4 + \frac{m_\phi^2}{24} T^2 - \frac{1}{12\pi} m_\phi^3 T \\ &- \frac{\mu^{-2\epsilon}}{2(4\pi)^2} m_\phi^4 \left[\ln \left(\frac{\bar{\mu} e^\gamma}{4\pi T} \right) + \frac{1}{2\epsilon} \right] + \frac{\zeta(3)}{3(4\pi)^4} \frac{m_\phi^6}{T^2} + \mathcal{O} \left(\frac{m_\phi^8}{T^4} \right) + \mathcal{O}(\epsilon) \end{aligned} \quad (7)$$

where $\ln \bar{\mu}^2 \equiv \ln(4\pi\mu^2) - \gamma$ with μ being the scale parameter of dimensional regularization; γ is an Euler's constant; ϵ is a regularization parameter of dimensional regularization; $\zeta(3)$ is zeta function evaluated at 3. For the contributions to the CC, one can note the ϕ -independent terms: the first two leading order terms scale $\sim T^4$ and $\sim T^2$. To extend the discussion to an FLRW background, let us extend the system to a curved background.

$$S_{ren} = \frac{1}{\kappa^2} \int d^4x \sqrt{\gamma} (R - 2\Lambda_1) - \int d^4x \sqrt{-g} \left(\frac{1}{2} g^{\mu\nu} \partial_\mu \phi \partial_\nu \phi + V \right) \quad (8)$$

where $\kappa^2 = 16\pi G$ with G Newton's constant; κ^2 will be suppressed in some places. As well known, an FLRW background has a time-dependent temperature. Due to this, the standard finite-temperature cannot in general be directly applied. This issue has been recently addressed in [6]. For an FLRW background, the standard finite-T techniques can be applied with minor modifications. This is due to the special feature of an FLRW background (the

flat case in which we are interested) that the temperature scales as $\sim \frac{1}{a}$ and the scale factor happens to be a metric component:

$$ds^2 = -dt^2 + a(dx^2 + dy^2 + dz^2) \quad (9)$$

Therefore the temperature is annihilated by the covariant derivative and the upshot is that the temperature T appearing in the results such as (17) can simply be replaced by the time-dependent one $T(t)$. The result (17) thus implies

$$\Lambda \equiv \Lambda_1 + \frac{\Lambda_2}{a^4} + \frac{\Lambda_3}{a^2} + \dots \quad (10)$$

where Λ_2 and Λ_3 are numerical constant introduced as part of the definition of Λ . Ω_{Λ_2} and Ω_{Λ_3} are then introduced as the corresponding density parameters, which implies the modified form of the Hubble constant given in (21).

A natural question arises as to whether Ω_{Λ_2} and Ω_{Λ_3} could be absorbed into existing parameters such as the radiation density Ω_r and curvature density Ω_K , respectively, given their similar scaling behaviors. However, this is not possible: as shown above, the perturbations arising from finite-temperature QFT effects are of a fundamentally different nature from those associated with radiation or curvature. For instance, Ω_K appears at the classical level in the standard Λ CDM cosmology whereas Ω_{Λ_3} has a strictly quantum origin. Hence, Ω_{Λ_2} and Ω_{Λ_3} are independent and not reducible to existing terms. To explicitly see this simplest possible way, consider the Einstein–Hilbert action including a cosmological constant:

$$\mathcal{L} = \frac{1}{\kappa}(-2\Lambda_1 + R) \quad (11)$$

We expand the metric $g_{\mu\nu}$ around a background solution $g_{0\mu\nu}(K)$ such that $g_{\mu\nu} \equiv h_{\mu\nu} + g_{0\mu\nu}(K)$, where the background is given by:

$$ds^2 = a^2 \left[d\mathbf{x}^2 + K \frac{(\mathbf{x} \cdot d\mathbf{x})^2}{1 - K\mathbf{x}^2} \right] \quad (12)$$

By substituting this expansion into the action and taking the $h_{\mu\nu}$ -variation, one obtains the field equations. In this context, the background curvature parameter K appears in multiple locations within the resulting equations. This explains why the density parameter Ω_K , defined as

$$\Omega_K \equiv -\frac{K}{a_0^2 H_0^2} \quad (13)$$

enters the standard cosmological equations through several distinct channels. In contrast, the parameter Ω_{Λ_3} has an entirely different physical origin. When finite-temperature one-loop corrections are incorporated, the cosmological constant Λ_1 is shifted schematically as:

$$\Lambda_1 + \Lambda_2 \frac{1}{a^4} + \Lambda_3 \frac{1}{a^2} + \dots \quad (14)$$

Unlike Ω_K , the parameter Ω_{Λ_3} originates exclusively from the cosmological-constant term of the off-shell one-loop effective action. Following a standard linearized analysis of gravity

coupled with hydrodynamic matter, it enters the Hubble parameter H .³ While Ω_K (once kept) and Ω_{Λ_3} appear only in the combination $\Omega_{\Lambda_3} + \Omega_K$ within the expression for H , these parameters are fundamentally non-redundant

- **Origins:** One is geometric (curvature), while the other stems from quantum corrections (loop effects).
- **Appearances:** They enter the action and resulting field equations through distinct mathematical terms.

The non-degeneracy of these parameters has been explicitly verified in Appendix A through numerical analysis using a modified version of the CLASS code.

As for Ω_{Λ_2} , one might also think that finite-temperature quantum loop-induced contributions to the CC - especially those involving photons and neutrinos - are redundant, since these are already accounted for as radiation. However, this conflation is misleading. Radiation arises from physical, on-shell particles (e.g., photons, neutrinos) through, say, kinetic theory physics, whereas the contributions under consideration are due to virtual particles in loop corrections. The finite-temperature effects we consider are analogous to vacuum energy contributions induced by loop effects in QED photon and electron fields. Radiation density, on the other hand, pertains to the energy density of physical photons and neutrinos. Therefore, the finite-temperature effects we consider are not included in the conventional radiation density and must be accounted for separately.

To be precise, let us examine a system governed by Boltzmann kinetic theory - such as a photon gas - interacting with a scalar field (e.g., the Higgs field) in a curved spacetime background. The total action of the system is given by

$$S = S_{EH} + S_{sf} + S_{kin}, \quad (15)$$

where S_{EH} represents the Einstein-Hilbert action with a cosmological constant, S_{sf} is the scalar field action, and S_{kin} accounts for the kinetic sector. While the explicit form of S_{kin} is known in certain models (see, e.g., [32, 33]) - such as that of an ideal gas - it will not be needed for our current purposes. The associated metric field equation contains the stress-energy tensor:

$$T^{\mu\nu} = \frac{1}{\sqrt{-g}} \sum_n \delta^3(x_n(t) - x) p_n^\mu(t) p_n^\nu(t) E_n(t). \quad (16)$$

To avoid unnecessary complications, we assume a fixed, non-dynamical background metric. Our primary interest lies in the T^4 -scaling (where T denotes the temperature) behavior relevant to Ω_{Λ_2} . The conventional analysis focuses exclusively on the classical thermodynamics

³The fluctuations $\delta\rho_{\Lambda_2}$ and $\delta\rho_{\Lambda_3}$ are neglected due to their suppressed nature - being both quantum in origin and small variations. Thus, their influence is minimal, and Ω_{Λ_2} and Ω_{Λ_3} effectively appear only within the modified Hubble parameter H . (This statement holds at the level of approximation adopted in the present work. At higher orders, additional terms such as $\Lambda R_{\mu\nu} R^{\mu\nu}$ are expected to appear.) In contrast, Ω_K and Ω_r directly contribute to the fluctuation equations and plays a significant role in the evolution of perturbations. In this work, Ω_{Λ_2} and Ω_{Λ_3} are treated phenomenologically, and their inclusion is justified by consistency with numerical results. (Theoretically, these parameters can be computed from first principles via the renormalization procedure. However, finite renormalization freedom necessitates experimental inputs like the present one to fix their values.)

of the kinetic system, which leads to the well-known exact T^4 -dependence of the energy density - see, for example, footnote 1 in section 3.1 of [11]. In contrast, the focus of this work is on quantum field-theoretic effects originating from the scalar field sector S_{sf} (as well as from other Standard Model particles and the graviton in the full description, which do not qualitatively alter the conclusions) at finite temperature. Importantly, such scalar fields cannot be treated as radiation due to their large masses; instead, their contributions to the cosmological constant arise through virtual processes, specifically vacuum bubble diagrams. To be concrete, consider the scalar sector. The one-loop correction to the classical (more precisely, renormalized) action takes the form

$$\begin{aligned} \not\int \frac{1}{2} \ln(K^2 + m^2) &= -\frac{\pi^2}{90} T^4 + \frac{m^2}{24} T^2 - \frac{1}{12\pi} m^3 T \\ -\frac{\mu^{-2\epsilon}}{2(4\pi)^2} m^4 &\left[\ln\left(\frac{\bar{\mu} e^\gamma}{4\pi T}\right) + \frac{1}{2\epsilon} \right] + \frac{\zeta(3)}{3(4\pi)^4} \frac{m^6}{T^2} + \mathcal{O}\left(\frac{m^8}{T^4}\right) + \mathcal{O}(\epsilon) \end{aligned} \quad (17)$$

where $\ln \bar{\mu}^2 \equiv \ln(4\pi\mu^2) - \gamma$; γ is an Euler's constant; $\epsilon \equiv \frac{4-D}{2}$. This expression represents an infinite series expansion in powers of temperature, with the leading contribution scaling as T^4 . Importantly, this term explicitly shifts the classical cosmological constant (CC) and is distinct from the T^4 contribution arising from the kinetic sector discussed earlier.

2.2 Modification of CLASS

With the conceptual framework established in Section 2.1, we now turn to the implementation of these ideas in CLASS. In its default configuration, CLASS evolves a cosmological model derived from the action

$$S = S_{\text{CC}} + S_{\text{EH}} + S_{\text{kin}}, \quad (18)$$

where S_{CC} denotes the cosmological constant term, S_{EH} is the Einstein–Hilbert action, and S_{kin} collectively represents the kinetic theory terms for matter and radiation. We modify CLASS to accommodate the extended system in which the standard cosmological constant contribution, denoted by Λ_1 , is replaced by the effective quantity Λ defined in Eq. (10).

The Λ CDM model (see [11,12] for reviews) assumes a spatially flat or nearly flat Universe, with a cosmological constant representing dark energy. It successfully explains the large-scale structure of the Universe, CMB observations, and galaxy formation. The model involves six primary parameters (or seven if the curvature density parameter Ω_K is included), which govern the composition and evolution of the Universe. These parameters are:

$$h, \quad \omega_b, \quad \omega_{\text{cdm}}, \quad A_s, \quad n_s, \quad \tau_{\text{reio}}. \quad (19)$$

Their definitions and cosmological roles are summarized in Table 1.

The CLASS code [16,17] is a computational tool used to solve the Boltzmann equations and generate the power spectra of cosmological observables within the Λ CDM framework. Once the cosmological parameters are specified, CLASS produces the relevant observables accordingly. However, when considering QG effects at finite temperatures, modifications to this standard framework become necessary. These arise due to the temperature dependence

Parameter	Description
h	The dimensionless Hubble parameter, which determines the current expansion rate of the Universe. Its value is crucial for estimating the age and size of the Universe.
ω_b	The baryon density parameter, representing the fraction of the Universe's energy density in the form of ordinary matter, "baryons".
ω_{cdm}	The cold dark matter density parameter, indicating the energy density contribution from non-relativistic, non-baryonic dark matter.
A_s	The amplitude of the primordial scalar perturbations, which parameterizes the magnitude of the initial density fluctuations.
n_s	The spectral index of the primordial perturbations, describing the scale dependence of the primordial power spectrum.
τ_{reio}	The optical depth to reionization, quantifying the degree of suppression of CMB anisotropies due to scattering by free electrons produced during reionization.
Ω_K	The curvature density parameter, accounting for the spatial curvature of the Universe. A value of $\Omega_K = 0$ implies a flat Universe, while positive or negative values suggest open or closed spatial geometry.

Table 1: Summary of the cosmological parameters

of QG effects, which become relevant at high energies and lead to shifts in cosmological parameters. Among these, the most prominent is the cosmological constant Λ (denoted as Λ_1 in the present context), which becomes temperature-dependent due to quantum effects [4–6].⁴

Referring to [6] and prior studies on the 1PI effective action for the Standard Model coupled to gravity, we find that the expression for the Hubble parameter $H(t)$ is modified. The original expression, as adopted in [11], is

$$\begin{aligned}
H &= H_0 \left[\Omega_M \left(\frac{T}{T_{\gamma_0}} \right)^3 + \Omega_R \left(\frac{T}{T_{\gamma_0}} \right)^4 \right]^{\frac{1}{2}} \\
&= 7.204 \times 10^{-19} T^{\frac{3}{2}} \sqrt{1.523 \times 10^{-5} T + \Omega_M h^2}.
\end{aligned} \tag{20}$$

where T denotes the temperature. (In [11], both the Ω_{Λ_1} and curvature density parameter are neglected for their small contributions.) The modified CLASS implementation [26],⁵

⁴These works extend earlier studies of foliation-based gravity quantization at finite temperature [34–38]. In particular, the gauge $K = 0$ (or more generally $K = K_0$), where K is the trace of the second fundamental form, plays a key role [37]. This approach parallels Witten's recent treatment in [39].

⁵The code was obtained in collaboration with K.-T. Cho and M.-S. Lee.

includes finite-temperature corrections, yielding the following form:

$$H = 7.204 \times 10^{-19} T^{\frac{3}{2}} \sqrt{1.523 \times 10^{-5} T + \left(\frac{2.725}{T}\right)^3 \Omega_{\Lambda_1} h^2 + \Omega_M h^2 + \frac{T}{2.725} \Omega_{\Lambda_2} h^2 + \frac{2.725}{T} \Omega_{\Lambda_3} h^2} \quad (21)$$

In the approximation adopted in the present work, this is the only location where Ω_{Λ_2} and Ω_{Λ_3} appear.

3 Numerical analysis

Our analysis employs a modified version of CLASS incorporating the quantum gravity modifications previously described. The parameter space exploration proceeds in two distinct phases. First, we conduct a comprehensive brute-force scan across eight cosmological parameters spanning generous ranges to ensure complete coverage of the parameter space. By these comprehensive scans tens of millions of data points are obtained. Following this initial broad exploration, we implement a refined search strategy focusing on regions that minimize the Euclidean distance (see the comments below) between our computed power spectra and the Planck dataset. This targeted approach yields significantly improved precision, with the minimal achieved distance of 26.83 corresponding to parameter values largely consistent with existing literature.⁶ Notably, the optimal solution features a negative value for Ω_{Λ_2} , a result that finds natural explanation through dimensional regularization in the renormalization procedure.

The methodology described above⁷ departs significantly from the standard Bayesian parameter inference employed by the Planck collaboration [18], and several comments are in order to clarify this choice. The primary motivation for adopting a non-standard, deterministic approach lies in the behavior of the newly introduced parameters, particularly Ω_{Λ_2} . Although theoretical estimates for the magnitude of Ω_{Λ_2} are possible and in fact necessary as a preliminary step, it was observed in [15] that these estimates overshoot the best-fit value by several orders of magnitude (a possible explanation for this mismatch is discussed in [15]) - a discrepancy that results in power spectra incompatible with observational data. Given the lack of reliable priors and the computational expense of performing full Bayesian inference over such a vast and poorly constrained parameter space, we instead adopted an iterative trial-and-error method. This involved progressively reducing Ω_{Λ_2} and performing wide parameter scans until convergence toward the observed Planck 2018 power spectrum was achieved. Although this procedure lacks formal statistical underpinnings (see the conclu-

⁶To give a sense of the accuracy associated with this number, the distance between the 2018 Planck curve and one generated by CLASS using the `default.ini` settings is approximately 75. Any curve with a distance to the Planck curve of less than approximately 1000 is visually indistinguishable from it.

⁷While we use frequentist inference, as noted in [15], this approach deviates from traditional frequentist methods: cosmological parameters are treated as input variables in the regression framework, with the polynomial coefficients taking on the role of statistical parameters instead of the cosmological parameters themselves. The resulting model serves as a surrogate, approximating the relationship between cosmological parameters and observables.

sion for further discussion), it proved effective in identifying the correct order of magnitude for Ω_{Λ_2} .

Our analysis leveraged the unbinned theoretical power spectrum file provided by the Planck 2018 collaboration:

`COM_PowerSpect_CMB-base-plikHM-TTTEEE-lowl-lowE-lensing-minimum-theory_R3.01.txt`.

As this dataset represents a smooth, noise-free theoretical prediction sampled at integer multipoles and lacks an associated covariance matrix, it further justifies our departure from likelihood-based methods that rely on detailed error modeling. In contrast, the observed spectra (given, e.g., in `COM_PowerSpect_CMB-TT-full_R3.01.txt`) are binned and require covariance information to be properly interpreted, which was not necessary for our purposes. A major advantage of our approach is its computational efficiency. The entire parameter scan process was executed within the CLASSy framework, with only a minimal external script used to calculate and rank distance measures - an operation that completes nearly instantaneously. In comparison, integrating additional tools like Cobaya or MontePython for full Bayesian inference increased runtime by a factor of six to eight. Given that our data collection alone required over three months, the reduction in computational overhead was a decisive factor. While our trial-and-error method is not a substitute for a rigorous statistical analysis, it enables rapid, resource-efficient exploration of the parameter space. Once a viable range for Ω_{Λ_2} is identified, more focused Bayesian scans using Cobaya become both feasible and significantly less time-consuming.

To complement and enhance the efficiency of our parameter space exploration, we implement advanced ANN techniques. Various numerical calculations and machine learning methods have been recently applied to the physics of black hole solutions [40–43]. These machine learning methods enable precise identification of optimal parameter coordinates while maintaining computational tractability across the challenging eight-dimensional parameter space.

Let us explore the estimation of the distance based on the currently established parameters as well as the finite-T induced ones, Ω_{Λ_2} and Ω_{Λ_3} . Throughout this section, the prediction accuracies are translated into the performance of the ANN-based method in detecting the minimum distance to the 2018 Planck curve from statistical populations in the presence of the finite-T effects.

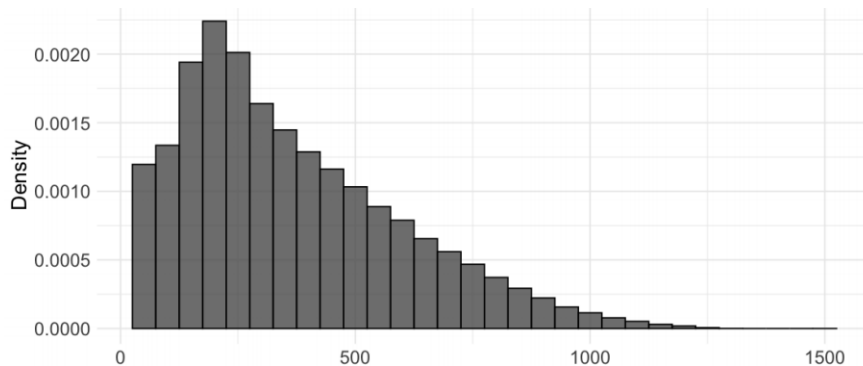


Figure 2: Sampling distribution of the distance values based on 8 cosmological parameters.

The numerical analyses evaluate the distance between the 2018 Planck curve and 7-parameter and 8-parameter ones using 459,912 and 335,985 data points, respectively. These data points are computed over equally spaced grids spanning the domain of the two approaches. These two data sets are considered as two statistical populations corresponding to the two estimation methods. We consider the response variable y , representing the distance function $y = f(\mathbf{x})$, which measures the deviation of the proposed estimation methods from the 2018 Planck power spectrum. In this setup, the parameters of the estimation methods were treated as explanatory variables $\mathbf{x} = (x_1, \dots, x_J)$, where $J = 7$ for the 7-parameter model and $J = 8$ for the 8-parameter model. Using this framework, the ML model maps the cosmological parameters to the distance function, enabling us to evaluate and predict the performance of the two estimation methods. This approach was particularly valuable for assessing the accuracy of the proposed methods, in the presence or absence of Ω_{Λ_2} .

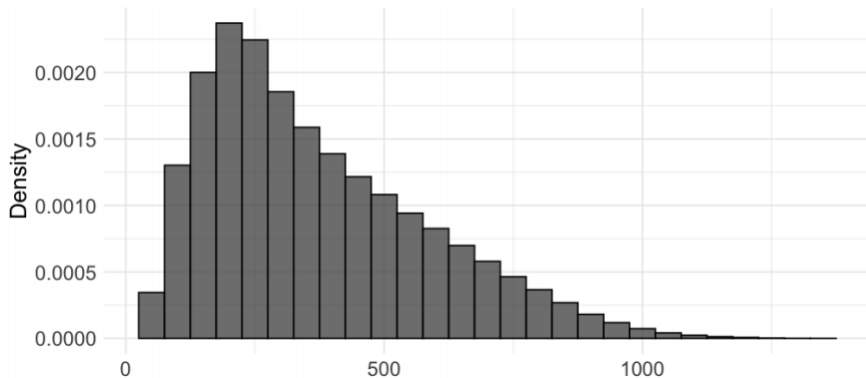


Figure 3: Sampling distribution of the distance values based on 7 cosmological parameters.

Figs. 2 and 3 show the sampling distributions of the distance responses based on two statistical populations derived from the entire dataset in the presence and absence of the leading-order finite-T effect parameter, Ω_{Λ_2} , as input data in computation of the distance responses. Table 2 provides descriptive statistics for the distance distributions based on these two statistical populations. While the sampling distributions in Figs. 2 and 3 show that both data capture critical aspects of the distance response function, Table 2 highlights the clear advantage of the 8-parameter population. It achieves a smaller average distance to the 2018 Planck result, indicating higher accuracy of the 8-parameter estimation method. Note that this superiority of the 8-parameter method is achieved despite using fewer data points, nearly 100,000 fewer than the 7-parameter competitor and relying on a coarser grid. In contrast, the 7-parameter method, with finer grid sampling and more extensive data, falls short of the prediction accuracy attained by the 8-parameter method. This numerical comparison indicates the effectiveness of our proposed 8-parameter approach, demonstrating its ability to deliver better predictions with less computational effort and fewer resources.

In the following, we treat the output function as the distance between the estimation method and the 2018 Planck data. Hence, the superiority of the methods in predicting the distance function is translated into the superiority of the estimation methods in minimization of the distance response function based on the data generated from the distance function under the two statistical populations. To evaluate the performance of the methods in min-

Statistics	Distance population with Ω_{Λ_2} and Ω_{Λ_3}	Distance population with Ω_{Λ_3}
Size	335985	459912
Minimum	26.83	28.12
1st Quartile	186.97	203.91
Median	313.21	321.48
Mean	366.12	371.29
3rd Quartile	510.30	505.75
Maximum	1491.66	1335.36

Table 2: The five-number summaries of the distance statistical populations.

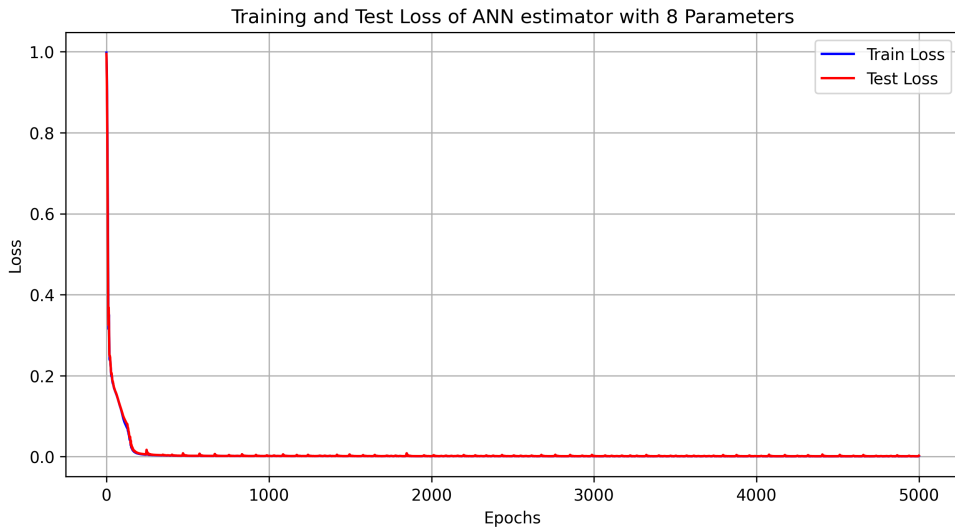


Figure 4: The training and validation loss functions of the proposed ANN method in estimating the distance response function based on eight cosmological parameters with over 5000 epochs.

imizing the distance response function, we identified 20,000 data points with the smallest distance values from each statistical population. From now on, we will focus on these two data sets as our statistical populations to find the minimum of the distances. Since the functional form of the distance from these statistical populations is unknown, first, one needs to predict the distance as a function of the cosmological features in \mathbb{R}^7 and \mathbb{R}^8 corresponding to the two statistical populations in absence and presence of Ω_{Λ_2} term, respectively. To do so, we applied ANNs to numerically predict the distance functions from these two statistical populations.

We train the ANNs-based model, described in section B.1 (see Fig. 11 for a schematic diagram of the trained ANNs), separately for the 7-parameter and 8-parameter statistical populations. For the 8-parameter population, we employ an ANN that begins with an input layer of eight nodes, one for each cosmological parameter, followed by four hidden layers, each containing 16 neurons. We use Rectified Linear Unit (ReLU) activation functions

throughout the hidden layers to obtain a robust capability for modelling complex, nonlinear relationships among the parameters in 8D. Before training, all input features are standardized to account for the broad range of magnitudes present in the different coordinates. To do so, each parameter is transformed to zero mean and unit variance. This step facilitates faster convergence and mitigates potential biases introduced by vastly different parameter scales. We split the dataset into 80% training and 20% test data sets to evaluate prediction performance to validate that model selection and hyperparameter tuning on unseen test data. The network is trained using the Adam optimizer with a learning rate of 0.001 with a mean squared error (MSE) loss function (B.3) over 5000 epochs. For fair comparisons, we train and compute the ANN-based prediction performance of the distance function using a 7-parameter statistics population under the same ANN configuration as described above. By combining a carefully standardized feature set, a structured architecture of hidden layers, and a well-tuned optimization, the ANNs effectively capture the dependencies underlying the distance response in both statistical populations.

Figs. 4 and 5 show the training and test loss values based on 8- and 7-parameter statistical populations, respectively. It is easy to see that the training and test loss functions resemble patterns very closely, confirming the ANN-based estimates could predict the underlying distance in both statistical populations. Comparison of Figs. 4 and 5 reveals an interesting contrast. Although the eight-parameter model is constructed from a more coarsely sampled statistical population, its ANN estimator’s test losses track the training losses more closely than the seven-parameter model. Consequently, the eight-parameter test loss converges faster, whereas the seven-parameter model shows a slight shortfall, evidenced by larger gaps between its training and test loss curves.

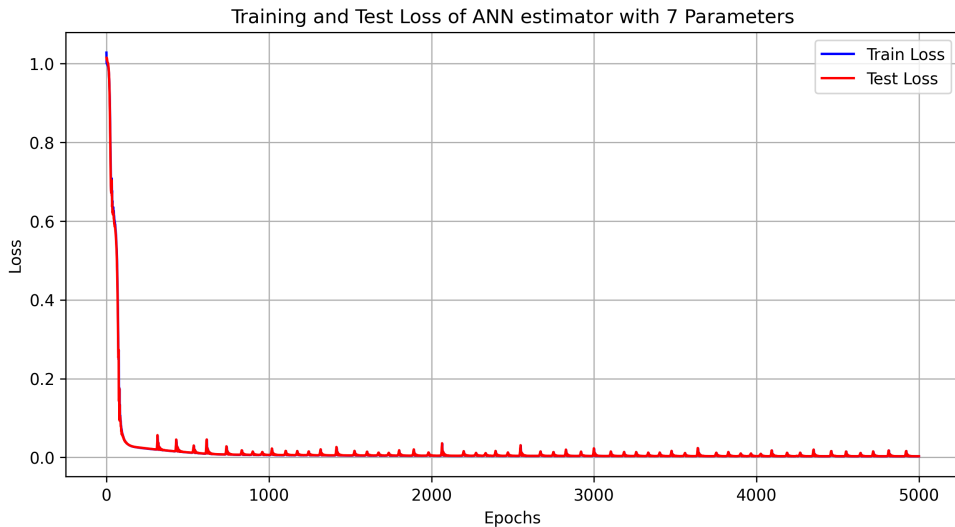


Figure 5: The training and validation loss functions of the proposed ANN method in estimating the distance response function based on seven cosmological parameters with over 5000 epochs.

To evaluate the reliability of the proposed ANN model, we conduct 500 independent replications of the ANN fitting procedure, as described earlier, each applying a similar 8-

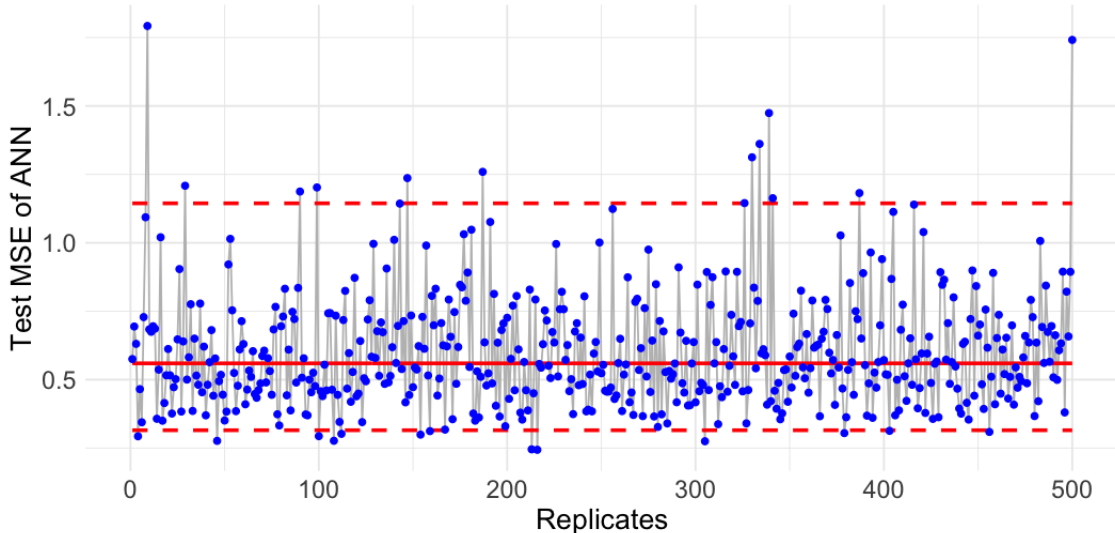


Figure 6: The blue points show the test MSEs of the proposed ANN model for estimating the distance response using eight cosmological parameters based on 500 random replicates. The red dashed lines mark the 95% confidence interval for the test MSEs (0.31,1.14), and the solid red line shows the median test MSE of 0.55.

parameter population. In each replication, the model is trained for 1000 epochs, and its predictive performance is assessed by computing the test MSE in estimating the distance function. The resulting 500 MSE values are then sorted to calculate both the median (50th percentile) and the empirical 95% confidence interval (CI), determined by the 2.5th and 97.5th percentiles. Fig. 6 displays all 500 MSEs as blue points, with the median MSE indicated by a solid red line and the 95% CI shown with dashed red lines. Despite the stochastic nature of ANN, the results demonstrate consistent performance across trials. The test MSEs fluctuate around a median of 0.55, with a relatively narrow 95% confidence interval ranging from 0.31 to 1.14. These findings highlight the robustness and accuracy of the proposed ANN method in predicting the distance function, even when trained with 1000 epochs.

The gradients to optimize the distance function are computed as described in section B.2. Subsequently, we employed the BFGS optimization algorithm to find the minimum of the objective function. Since the explicit form of the distance function is unavailable, a trained ANN was used as a surrogate model to approximate the function and compute the gradients numerically. Accordingly, we implemented the gradient-based optimization iteratively until the algorithm converged and the stopping criterion, given by $\|\nabla \mathcal{F}^L(\mathbf{x}, \hat{\boldsymbol{\theta}}_{opt})\|_2 < 10^{-7}$ is satisfied. (See Appendix B.) Once the ANN-based gradient optimization converges, the estimated optimal coordinates represent the minimum of the approximated distance function. Applying the optimization algorithm to the eight-parameter statistical population, the ANN-based optimization predicted a minimum distance of $y = 29.24$ with the corresponding parameter values: $(\Omega_{\Lambda_2}, \Omega_{\Lambda_3}, h, \omega_b, \omega_{cdm}, A_s, n_s, \tau_{reio}) = (-2.069 \times 10^{-8}, 0.00430, 0.6752, 0.02240, 0.1996, 2.1007 \times 10^{-9}, 0.9660, 0.05424)$. By using the same optimization configurations but considering the seven-parameter statistical population, the

ANN-based gradient optimization leads to a minimum Planck distance of $y = 32.09$. The corresponding parameter values at this minimum were:

$$(\Omega_{\Lambda_3}, h, \omega_b, \omega_{cdm}, A_s, n_s, \tau_{reio}) = (0.0023356, 0.6769, 0.2237, 0.1199, 2.0988 \times 10^{-9}, 0.9658, 0.05396).$$

By comparing the optimization results under the two statistical populations, we observe that the ANN-based estimate of the eight parameter model attains a lower minimum for the distance function. One can then apply the feature ablation method reviewed in section B.3 to evaluate the relative importance of Ω_{Λ_2} , compared to other established cosmological parameters. Since the explicit form of the distance function is not available, we employed feature ablation using ANNs to estimate its impact in two feature importance numerical studies.

We begin by performing an analysis by using ANNs to model the distance function across its entire domain. To construct a comprehensive dataset, we merge the 8-parameter statistical population with a 7-parameter population, setting $\Omega_{\Lambda_2} = 0$ in the latter. This integration resulted in a combined dataset of 795,897 data points. As described earlier, the ANN architecture consists of four hidden layers with 16 neurons each and is trained for 5000 epochs. The dataset is randomly partitioned into 80% training and 20% testing subsets to assess predictive performance. The ANN is then trained to approximate the distance response function over the full dataset. For the ablation study, we remove one input feature at a time, retrain the ANN, and evaluate the resulting change in test MSE. Table 3 presents the test MSEs for both the full model and each reduced model. Despite the high nonlinearity of the distance function ranging from 0 to 1491, the full model achieves an average test MSE of only 4.95, demonstrating the ANN’s strong prediction performance to capture the global structure of the function. Also, we observe that removing Ω_{Λ_2} led to a greater increase in test MSE compared to removing some of the established parameters, indicating that Ω_{Λ_2} plays a more significant role in predicting the Planck distance across the full domain than those.

Table 3: This result is based on the entire 700K data. MSEs of the full models and reduced models after feature removals using ANN models using 5000 epochs based 700k data points obtained by combining all 8- and 7-parameter statistical populations.

Feature Removed	MSEs using ANNs
Full Model	4.95018
Ω_{Λ_2}	5.74744
Ω_{Λ_3}	5.21219
h	189.192
ω_b	595.213
ω_{cdm}	31866.2
A_s	35877.0
n_s	728.578
τ_{reio}	10252.8

In the next feature ablation analysis, the aim is to evaluate the individual contributions of each input feature to the minimum values of the distance function. Since the objective is to identify the function’s minimum, we focus on a subset of 5000 data points corresponding to the lowest distances from the combined population. We apply the ANNs by using the

same architecture as in the previous analysis, but train with 5000 epochs. For uncertainty quantification, we employ 50-fold cross-validation. In each of the 50 runs, 49 folds (4900 data points) are used for training the ANN, and the remaining fold (100 data points) is used for testing. This process is repeated, so that each fold serves once as the test set. In each run, the test MSE for both the full model and reduced models are calculated, each constructed by removing a single feature. This yields 50 MSE values for the full model and for each reduced model. Fig. 7 presents the results of this analysis, where the height of each blue

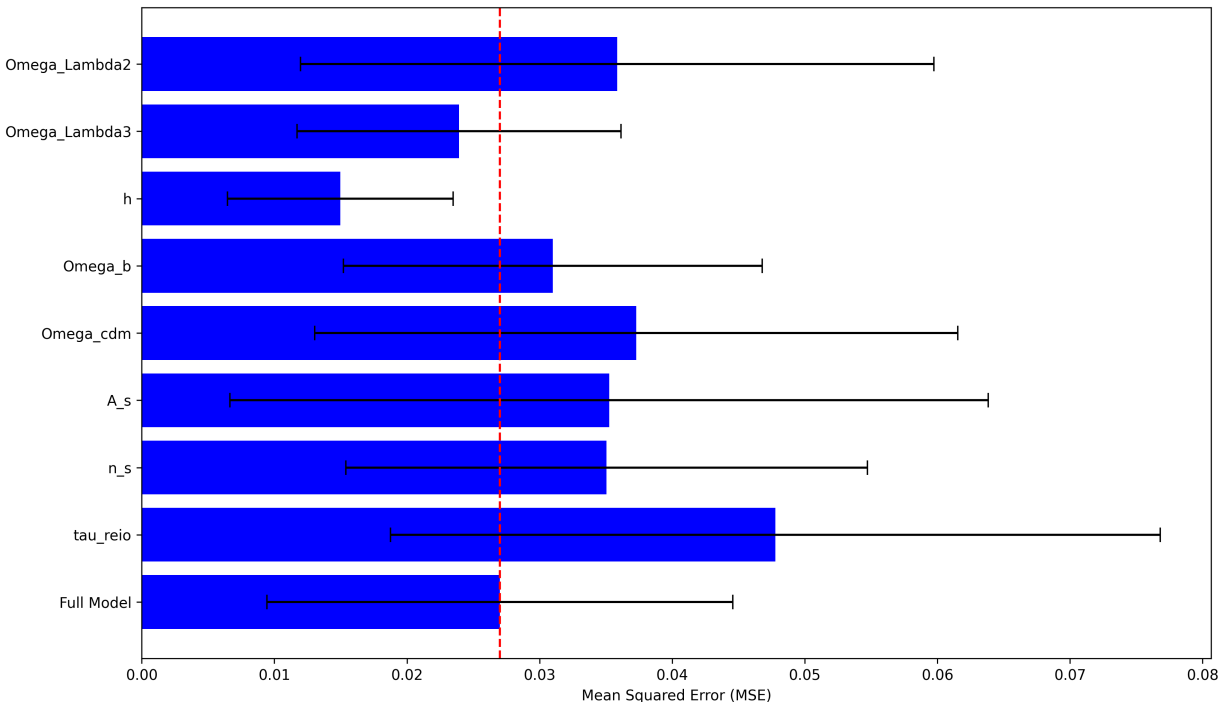


Figure 7: This result is based on the first 5000 shortest distances. Test MSEs of the full and reduced ANN models for predicting the distance function. Each bar represents the mean MSE along with its 95% confidence interval, computed across 50 folds. Reduced models exclude one input parameter at a time to assess its impact on prediction performance.

bar shows the mean test MSE and the black lines denote the 95% confidence intervals. The variation in MSE across reduced models reveals that the features contribute unequally to the ANN’s performance in predicting the minimum distance. In addition, removing the feature Ω_{Λ_2} increased the average test MSE by approximately 25% compared to the full model, indicating its strong influence. Moreover, when comparing Ω_{Λ_2} to some of the parameters, we observe that the model with Ω_{Λ_2} has a greater impact on model accuracy.

Figure 7 presents a local sensitivity analysis based on a computationally intensive numerical experiment. Its purpose is to examine the relative importance of each parameter in achieving the minimum distance - essentially identifying which parameters are most critical for finding the ‘optimal’ values. This analysis focuses specifically on how individual parameters influence the optimization process near that optimum point. Table 3, by contrast, is based on a global analysis using all 700,000 data points across the full parameter space

(combining both the 7-parameter and 8-parameter models). The objective of Table 3 is not optimization, but rather to assess which parameters are most important for accurately estimating the entire Planck curve over its full domain in \mathbb{R}^8 . Due to the large dataset size, the Artificial Neural Network (ANN) was trained only once for Table 3. Parameter importance was then evaluated using a 'leave-one-out' strategy: each parameter was excluded in turn, and the resulting increase in estimation error was recorded. The magnitude of this error increase serves as a quantitative measure of each parameter's contribution to the accurate global reconstruction of the Planck curve.

The results shown in Table 3 and Fig. 7 suggest that Ω_{Λ_2} and Ω_{Λ_3} play an important role in determining the fine structure of the curve. Table 3 shows that the large-scale shape of the curve is primarily determined by the standard parameters. However, once attention is restricted to curves that closely match the Planck 2018 result, the parameters Ω_{Λ_2} and Ω_{Λ_3} become essential.

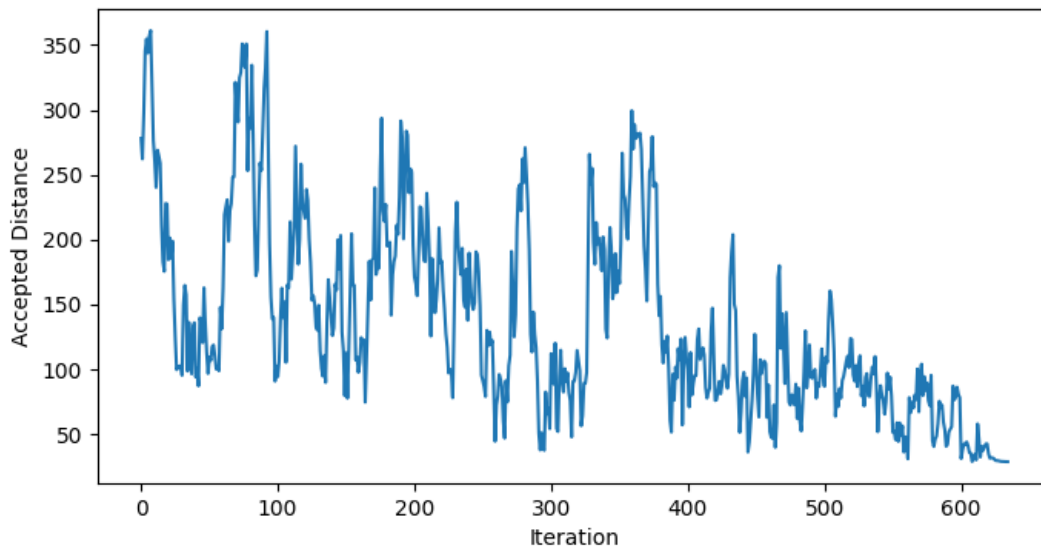


Figure 8: The trace plot of the Markov Chain Monte Carlo of the accepted minimum distances obtained by the stochastic simulated annealing based on ANNs.

With the significance of Ω_{Λ_2} confirmed through feature ablation, we now use the simulated annealing approach of section B.4. This method is applied to the statistical population with the quantum gravity feature to determine the minimum of the distance function. The optimization problem involves eight input parameters, with the objective function being unavailable in an explicit analytic form. Instead, it must be approximated stochastically through forward and backward computations of an ANN, as described earlier. Given the integration of multiple numerical methods, it is crucial to account for the sampling variability of parameter estimates and the numerical measurement errors in identifying the minimum. To address this challenge, we employed the stochastic simulated annealing approach within a probabilistic framework.

The optimization process begins with an initial random solution, and perturbations are

introduced iteratively using a random walk Metropolis-Hastings algorithm to explore the parameter space. The initial temperature is set to $T_0 = 10^4$, and a cooling schedule is applied with a decay rate of $\alpha = 0.99$, gradually reducing the acceptance probability for worse solutions as the search progressed. The ANN predicts the distance response for proposed solutions throughout the optimization, guiding the SA algorithm toward the global minimum. The SA algorithm is run for 20,000 iterations, where 635 transitions are accepted. The results, illustrated in Fig. 8, show the MCMC sequence of accepted minimal distances obtained via ANN-based SA. Ultimately, the algorithm converges to the minimum distance value of $y = 28.8111$, with the corresponding optimal coordinates:

$$\begin{aligned} & (\Omega_{\Lambda_2}, \Omega_{\Lambda_3}, h, \omega_b, \omega_{cdm}, A_s, n_s, \tau_{reio}) \\ = & (-2.061 \times 10^{-8}, 0.00425, 0.6762, 0.0223, 0.1196, 2.1 \times 10^{-9}, 0.9664, 0.056). \end{aligned} \quad (22)$$

The SA algorithm efficiently explores the complex and noisy domain, with the ANN acting as a surrogate model to approximate the distance function. This ensures robustness in parameter estimation, effectively handling both numerical measurement errors in the method and the sampling variability of the estimated parameters.

4 Conclusion

In this study, we have incorporated finite-T QG effects to improve the fit to the CMB power spectrum. Our analysis reveals that the newly introduced density parameter, Ω_{Λ_2} , takes on a negative value - a result that arises naturally within the framework of renormalization using dimensional regularization. Meanwhile, the inclusion of the parameter Ω_{Λ_3} introduces additional flexibility in modeling the spatial curvature of the Universe.

We evaluated the effectiveness and robustness of ANN-based methods in estimating cosmological parameters. Our results demonstrate that ANNs are capable of capturing complex nonlinear dependencies and accurately modeling cosmological data. Numerical experiments indicate that the introduction of finite-temperature-induced density parameters enhances predictive performance, enabling faster convergence and improved accuracy, even when training data is limited. This highlights the potential relevance of quantum gravitational corrections in refining cosmological predictions. Notably, our extensive numerical analysis revealed that finite-temperature corrections can have a more substantial impact on predictive accuracy than some well-established cosmological parameters. To further optimize parameter estimation, we incorporated a simulated annealing algorithm guided by ANN predictions. This stochastic optimization strategy efficiently navigates the parameter space while accounting for numerical uncertainties in the distance function, producing robust estimates for the underlying cosmological parameters.

A central motivation of this work was to explore whether finite-temperature quantum-gravity corrections could help alleviate the Hubble tension [25]. While our findings do not resolve the tension outright (see, e.g., [44] for evidence of resolution in dynamical vacuum models), they suggest that higher-order finite-temperature effects may play a meaningful role, warranting further investigation. A key limitation of our present analysis is that, although simulated annealing identifies best-fit parameters, it does not provide likelihood curvature

and therefore cannot yield statistical uncertainties; moreover, because the distribution of the distance function is unknown, a classical likelihood cannot be constructed without imposing arbitrary assumptions.⁸ To avoid these issues, we reformulated the problem using an artificial neural network (ANN) trained to approximate the distance function across the high-dimensional parameter space in both the 7- and 8-parameter settings, thereby enabling ANN-based numerical optimization to locate the global minimum and the associated cosmological parameter estimates without assuming any particular distribution. To quantify uncertainty and assess the relative importance of each parameter, we implemented a numerical ANN-based feature-ablation procedure, which provides 95% confidence intervals for the prediction MSE and highlights the contribution of each cosmological parameter to the distance function; the resulting intervals are shown in Fig. 8. Looking ahead [45], implementing a full Bayesian inference analysis - using packages such as Cobaya or MontePython - will be a priority for statistically quantifying parameter constraints and validating the ANN-guided results presented here, and a dedicated comparison with polarization data will be essential for further solidifying and refining these conclusions.

Acknowledgments

Armin Hatefi acknowledges the Natural Sciences and Engineering Research Council of Canada (NSERC). Ehsan Hatefi thanks Jose Luis Alvarez-Perez, Pablo Diaz Villar, Philip Siegmann, and Luis Alvarez-Gaume for their helpful discussions and support. Ehsan Hatefi also thanks Enrico Trincherini, Augusto Sagnotti, and the Scuola Normale Superiore in Pisa for their support. Ehsan Hatefi is supported by his International Maria Zambrano Grant from the Ministry of Spain.

⁸In addition, not all digits reported in the Planck minimum-theory spectrum file `COM_PowerSpect_CMB-base-plikHM-TTTEEE-lowl-lowE-lensing-minimum-theory_R3.01.txt` are expected to be statistically significant, which limits the meaningful numerical precision of any parameter comparison.

A Demonstration of non-degeneracy of Ω_{Λ_3} and Ω_K

In this appendix, we explicitly demonstrate the non-degeneracy of Ω_{Λ_3} and Ω_K . Let us choose $(\Omega_{\Lambda_2}, \Omega_{\Lambda_3}, h, \omega_b, \omega_{cdm}, A_s, n_s, \tau_{reio})$ as follows:

$$\begin{aligned} \Omega_{\Lambda_2} &= 0.00000017 \\ h &= 0.67810, \omega_b = 0.02238280, \omega_{cdm} = 0.1201075, A_s = 2.100549 \times 10^{-9}, n_s = 0.9660499, \tau_{reio} = 0.054308. \end{aligned} \quad (\text{A.1})$$

As for $\Omega_{\Lambda_3}, \Omega_K$, let us try the following two combinations:

$$\begin{aligned} \Omega_{\Lambda_3} &= 0.001, \Omega_K = 0 \\ \Omega_{\Lambda_3} &= 0, \Omega_K = 0.001. \end{aligned} \quad (\text{A.2})$$

Figs. 9 and 10 show the first 10 columns of the `cl_lensed.dat` files obtained by running corresponding `ini` files.

#	1:1	2:TT	3:EE	4:TE	5:BB	6:phiphi
2		1.378104946502e-10	4.179361151157e-15	3.502702242376e-13	2.319738340897e-19	8.225514557797e-09
3		1.303342247149e-10	5.353811982313e-15	3.939060584539e-13	4.640381216727e-19	5.067319193462e-09
4		1.232864835582e-10	4.627643731732e-15	3.684831525049e-13	7.735962662118e-19	3.523671626296e-09
5		1.180105834440e-10	3.085022852206e-15	3.138901887809e-13	1.160764429291e-18	2.630885687531e-09
6		1.143925101258e-10	1.724530386982e-15	2.528873226144e-13	1.625684082059e-18	2.055944156475e-09
7		1.120317494019e-10	9.328561006918e-16	1.986330396070e-13	2.168519665325e-18	1.659461872213e-09
8		1.106544028552e-10	6.035194844781e-16	1.568844059056e-13	2.789455922855e-18	1.372266171324e-09
9		1.100175237064e-10	4.856881629445e-16	1.289232939281e-13	3.488694977348e-18	1.156138964372e-09
10		1.098800100619e-10	4.147989427627e-16	1.134408209145e-13	4.266453224216e-18	9.885630521500e-10
11		1.101938800791e-10	3.496137256105e-16	1.077913613009e-13	5.122958121612e-18	8.330051246885e-10

Figure 9: $\Omega_{\Lambda_3} = 0.001, \Omega_K = 0$.

#	1:1	2:TT	3:EE	4:TE	5:BB	6:phiphi
2		1.378540251058e-10	4.158906085757e-15	3.485569500311e-13	2.309543399470e-19	8.204874158737e-09
3		1.303786580330e-10	5.340064466534e-15	3.929620147597e-13	4.619978491321e-19	5.054919097234e-09
4		1.233276672604e-10	4.621265102713e-15	3.682249526745e-13	7.701930186592e-19	3.517263079701e-09
5		1.180598981544e-10	3.084531745791e-15	3.137857604931e-13	1.155654463603e-18	2.625419055846e-09
6		1.144318409399e-10	1.727454463706e-15	2.530955278052e-13	1.618521858037e-18	2.051696606018e-09
7		1.120885542675e-10	9.359759118138e-16	1.989655349612e-13	2.158957676329e-18	1.655999298605e-09
8		1.107111974734e-10	6.058147040793e-16	1.572413873635e-13	2.777144614936e-18	1.369353000368e-09
9		1.100540448422e-10	4.873124734090e-16	1.292428117910e-13	3.473282759980e-18	1.153643354028e-09
10		1.099352998217e-10	4.159936877124e-16	1.136553853774e-13	4.247586571380e-18	9.863984234178e-10
11		1.102242675366e-10	3.502885231098e-16	1.078585839706e-13	5.100281757638e-18	8.311756409921e-10

Figure 10: $\Omega_{\Lambda_3} = 0, \Omega_K = 0.001$.

As these figures show, the entries for the two cases are distinct.

B Statistical methods

Let us review the statistical and ML techniques employed in the main analysis. In the present study, we employ ANNs to predict the distance between the 2018 Planck data [18] and data generated by the modified CLASS with input cosmological parameter values. This ANN-based model is further used for sensitivity analysis through feature ablation, as well as for probabilistic optimization of cosmological parameters. Fig. 11 represents the schematic

diagram of the ANNs with eight nodes in the input layer representing the eight cosmological parameters and four hidden layers, each with 16 nodes and the output layer with one node of the distance. Once the ANN is trained, we use gradient-based optimization to determine the set of covariates that minimize the predicted distance. We then explain the feature ablation strategy to discuss the relative importance of cosmological parameters in the predictions. Finally, we developed the ANN-based probabilistic optimization to find the minimum of the distance, considering the numerical measurement errors.

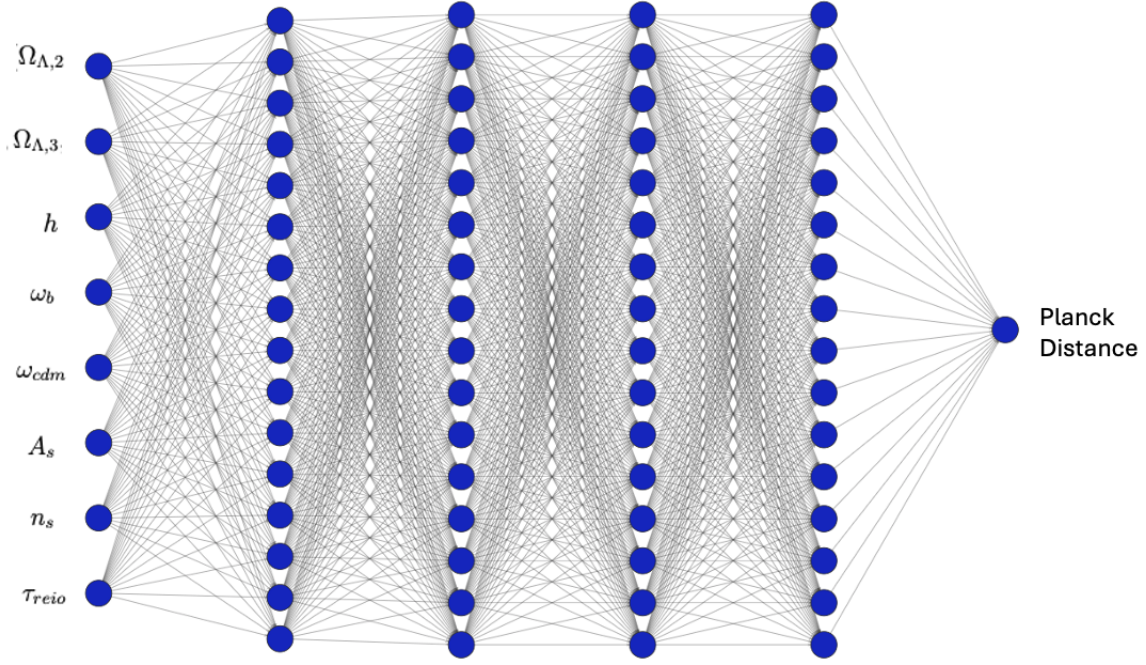


Figure 11: The schematic diagram of the trained ANNs mapping the eight cosmological parameters to the planck distance using four hidden layers, each hidden layer with 16 nodes.

B.1 Artificial neural networks

The ANN is a powerful estimation method mapping a set of input explanatory variables (henceforth called features) $\mathbf{x} = (x_1, \dots, x_{d_{in}})$ to an output (henceforth called response variable), that is $\mathbf{y} = (y_1, \dots, y_{d_{out}})$ [46]. The method estimates the relationship between the features and the response variable $\mathbf{y} = f(\mathbf{x}), f : \mathbb{R}^{d_{in}} \rightarrow \mathbb{R}^{d_{out}}$ through a network of layers consisting of interconnected neurons. The network architecture gets information from the input data. The information is then transferred between hidden layers and the activation functions to train the ANN. Once the ANN is trained, the method enables us to learn the relationship between features and response and predict the response function.

Let $\mathcal{F}^L(\mathbf{x}, \boldsymbol{\theta})$ represent a deep neural network with L layers that transforms an input from $\mathbb{R}^{d_{in}}$ into an output in $\mathbb{R}^{d_{out}}$, where d_{in} and d_{out} denote the dimensions of the input and output spaces, respectively. Suppose m_l represents the number of neurons in the l -th hidden layer of the ANN, where $m_0 = d_{in}$ and $m_L = d_{out}$ corresponds to the input and output layer sizes, respectively. Each layer l ($l = 1, \dots, L - 1$) is associated with a weight matrix

$\mathbf{W}^l \in \mathbb{R}^{m_l \times m_{l-1}}$, whose element $W_{j,k}^l$ denotes the weight connecting neuron j in layer l to neuron k in layer $l-1$. In addition, each layer uses a bias vector $\mathbf{b}^l \in \mathbb{R}^{m_l}$, where the j -th element, b_j^l , represents the bias term associated with the j -th neuron in layer l . Suppose $\boldsymbol{\theta} = \{\mathbf{W}^1, \dots, \mathbf{W}^L, \mathbf{b}^1, \dots, \mathbf{b}^L\}$ denotes the set of all unknown parameters of the ANN. Let \mathbf{M}^l denote the response from layer l before activation; hence \mathbf{M}^l is given by:

$$\mathbf{M}^l = \mathbf{W}^l \cdot \mathcal{F}^{l-1}(\mathbf{x}, \boldsymbol{\theta}) + \mathbf{b}^l, \quad \text{for } l = 1, \dots, L-1. \quad (\text{B.1})$$

We use the Rectified Linear Unit (ReLU) activation function $\sigma(z) = \max(0, z)$ in this work. Applying the activation function $\sigma(\cdot)$, the output of layer l is:

$$\begin{aligned} \mathcal{F}^l(\mathbf{x}, \boldsymbol{\theta}) &= \sigma(\mathbf{M}^l), \quad l = 1, \dots, L-1, \\ \mathcal{F}^L(\mathbf{x}, \boldsymbol{\theta}) &= \mathbf{M}^L. \end{aligned} \quad (\text{B.2})$$

To optimize the ANN's predictive performance, a loss function $\mathcal{J}(\mathcal{F}^L(\mathbf{x}, \boldsymbol{\theta}))$ is introduced to quantify the deviation of the predictions from the true target function. Here, the loss function is given by the mean squared loss function as

$$\mathcal{J}(\mathcal{F}^L(\mathbf{x}, \boldsymbol{\theta})) = \sum_{i=1}^n (f(\mathbf{x}_i) - \mathcal{F}^L(\mathbf{x}, \boldsymbol{\theta}))^2, \quad (\text{B.3})$$

where n denotes the size of the training data [47]. During training, a back-propagation is designed to find optimum solutions $\hat{\boldsymbol{\theta}}_{opt}$ which minimizes the loss function, that is $\hat{\boldsymbol{\theta}}_{opt} = \arg \min_{\boldsymbol{\theta}} \mathcal{J}(\mathcal{F}^L(\mathbf{x}, \boldsymbol{\theta}))$. The back-propagation algorithm calculates the errors from the output layer backward through the network by using the numerical gradients [48, 49]. The gradient of the loss with respect to the pre-activation output \mathbf{M}^l in layer l is computed recursively by

$$\frac{\partial \mathcal{J}(\mathcal{F}^L(\mathbf{x}, \boldsymbol{\theta}))}{\partial \mathbf{M}^l} = (\mathbf{W}^{l+1})^\top \cdot \frac{\partial \mathcal{J}(\mathcal{F}^L(\mathbf{x}, \boldsymbol{\theta}))}{\partial \mathbf{M}^{l+1}} \odot \sigma'(\mathbf{M}^l), \quad (\text{B.4})$$

where \odot denotes the element-wise Hadamard product, and $\sigma'(\cdot)$ is the derivative of the activation function. For the final layer, the gradient is computed by

$$\frac{\partial \mathcal{J}(\mathcal{F}^L(\mathbf{x}, \boldsymbol{\theta}))}{\partial \mathbf{M}^L} = \frac{\partial \mathcal{J}(\mathcal{F}^L(\mathbf{x}, \boldsymbol{\theta}))}{\partial \mathcal{F}^L(\mathbf{x}, \boldsymbol{\theta})} \odot \sigma'(\mathbf{M}^L). \quad (\text{B.5})$$

One can iteratively update the parameters using stochastic gradient descent to guarantee the convergence of the ANN toward an optimal solution and improve the accuracy of the predictive method. Once the ANN algorithm reaches the stationary point, the target response function can be predicted at any new input data \mathbf{x}_{new} by $\hat{\mathbf{y}}_{new} = \hat{f}(\mathbf{x}_{new}) = \mathcal{F}^L(\mathbf{x}_{new}, \hat{\boldsymbol{\theta}}_{opt})$. For further details, the readers are referred to [48, 50].

B.2 Gradient-based feature optimization with ANN

Once the ANN is trained, the next step is to determine the features that minimize the predicted response function $\mathbf{y} = f(\mathbf{x})$. This process can be reformulated as an optimization

problem in which the ANN-based estimate of the objective response function is minimized with respect to the features this time [51]. The gradient of the ANN output with respect to the input features is computed by:

$$\nabla \mathcal{F}^L(\mathbf{x}, \hat{\boldsymbol{\theta}}_{opt}) = \frac{\partial \mathcal{F}^L(\mathbf{x}, \hat{\boldsymbol{\theta}}_{opt})}{\partial \mathbf{x}}. \quad (\text{B.6})$$

This gradient is used to iteratively update the features in order to reach the optimal values that minimize the response function. We update the optimum features by:

$$\mathbf{x}^{(t+1)} = \mathbf{x}^{(t)} - \alpha \nabla \mathcal{F}^L(\mathbf{x}^{(t)}, \hat{\boldsymbol{\theta}}_{opt}) \quad (\text{B.7})$$

where α represents the step size tuning parameter used in the gradient descent process. We employ the Broyden-Fletcher-Goldfarb-Shanno (BFGS) optimization algorithm to find the optimal features [51, 52]. This method updates the input vector iteratively using the following equation:

$$\mathbf{x}^{(t+1)} = \mathbf{x}^{(t)} - \mathbf{H}_t^{-1} \left(\mathcal{F}^L(\mathbf{x}^{(t)}, \hat{\boldsymbol{\theta}}_{opt}) \right) \nabla \mathcal{F}^L(\mathbf{x}^{(t)}, \hat{\boldsymbol{\theta}}_{opt}), \quad (\text{B.8})$$

where $\mathbf{H}_t \left(\mathcal{F}^L(\mathbf{x}^{(t)}, \hat{\boldsymbol{\theta}}_{opt}) \right)$ represents an approximation of the Hessian matrix, which ensures a more accurate search direction compared to standard gradient descent. The algorithm is repeatedly alternated until the stopping rule of $\|\nabla \mathcal{F}^L(\mathbf{x}, \hat{\boldsymbol{\theta}}_{opt})\|_2 < \epsilon$ is satisfied, where $\|\cdot\|_2$ represents the ℓ_2 norm.

B.3 Feature ablation method

The feature ablation approach is an established method in ML that determines the relative importance of input features in predictive models. The method, as a leave-one-out technique, is applied iteratively to each coordinate in the domain of the objective function to find the contribution of each coordinate in the predictive performance of the underlying ML model [53]. To do that, the feature ablation method iteratively removes each feature and then evaluates the feature’s contribution to the performance of the underlying model.

Let $\{(\mathbf{x}_i, y_i); i = 1, \dots, n\}$ and $\{(\mathbf{x}_{j,test}, y_{j,test}); j = 1, \dots, m\}$ denote, respectively, the training and test data of sizes n and m from the representing the Planck distance response function $y = f(\mathbf{x})$ where $f : \mathbb{R}^d \rightarrow \mathbb{R}$. Because the objective response function is not explicitly available, as described in section B.1, we first predict the objective function using the ANN methods based on the training data. Let $\mathcal{F}^L(\mathbf{x}, \hat{\boldsymbol{\theta}}_{opt})$ denote the ANN-based estimate of the objective function $f(\mathbf{x})$. The prediction accuracy performance of the trained ANN estimate in the presence of all the input features is computed based on MSE using test data [47]. Accordingly, the ANN-based MSE is computed by

$$\text{MSE} \left(\mathcal{F}^L(\mathbf{x}, \hat{\boldsymbol{\theta}}_{opt}) \right) = \frac{1}{m} \sum_{j=1}^m \left(y_{j,test} - \mathcal{F}^L(\mathbf{x}_{j,test}, \hat{\boldsymbol{\theta}}_{opt}) \right)^2. \quad (\text{B.9})$$

Henceforth, the MSE (B.9) is called the full model MSE, showing the prediction error from an ANN-based estimate of the objective function using all the input features.

In the next step, we iteratively remove the individual feature $x_j, j = 1, \dots, d$ from the input design matrix. Let \mathbf{x}_{-j} denote the input features when the j -th feature x_j has been removed from the input data. We then train the ANN estimator of the objective function similar to the full model and find the ANN-based estimate $\widehat{f}(\mathbf{x}) = \mathcal{F}^L(\mathbf{x}_{-j}, \widehat{\boldsymbol{\theta}}_{opt})$. Accordingly, we compute the reduced model MSE in a similar vein to equation (B.9) using the test data in the absence of the x_j coordinates. Let $\text{MSE}(\mathcal{F}^L(\mathbf{x}_{-j}, \widehat{\boldsymbol{\theta}}_{opt}))$ denote the test MSE of the reduced model using data after removing the j -th coordinate for $j = 1, \dots, d$.

We then compute the feature ablation statistic after removing x_j by

$$\Delta\text{MSE}_j = \text{MSE}(\mathcal{F}^L(\mathbf{x}_{-j}, \widehat{\boldsymbol{\theta}}_{opt})) - \text{MSE}(\mathcal{F}^L(\mathbf{x}, \widehat{\boldsymbol{\theta}}_{opt})), \quad (\text{B.10})$$

where ΔMSE_j statistic shows the contribution of feature x_j in the prediction of the objective function $f(\mathbf{x})$, which can be viewed as the importance of feature x_j in the feature set [47]. Therefore, the ΔMSE_j statistic can be used as a numerical measure for selection and comparison between features in the prediction of the distance plank response as a function of the cosmological parameters $y = f(\mathbf{x})$. Accordingly, if $\Delta\text{MSE}_j > 0$, removing x_j increases the test MSE. This indicates the relative importance of the x_j feature in the prediction of the objective function. When $\Delta\text{MSE}_j \approx 0$, removing x_j has little effect on the performance of the ANN in predicting the objective function. Finally, when $\Delta\text{MSE}_j < 0$, removing x_j decreases MSE, suggesting the feature introduces noise in prediction with respect to other features. In other words, the feature x_j is redundant in prediction in the presence of the other variables. This feature ablation approach directly measures the significance of input planck parameters in predicting the planck distance function using $\mathcal{F}^L(\mathbf{x}, \widehat{\boldsymbol{\theta}}_{opt})$ from the ANN approach.

B.4 ANN-based simulated annealing

The simulated annealing (SA) algorithm is an effective numerical method for stochastic optimization problems. The goal of the method is to optimize objective function $y = f(\mathbf{x})$, where $\mathbf{x} \in \mathbb{R}^d$ denotes a set of input covariates. The process follows an iterative procedure where a candidate solution is perturbed at each iteration and then accepted or rejected as the solution through a probabilistic criterion [40, 54, 55].

The SA algorithm starts with an initial point \mathbf{x}_0 chosen randomly from the sample space and an initial temperature parameter T_0 . The algorithm also requires the cooling rate parameter to calibrate the temperature as the number of iterations increases. Like the Markov Chain Monte Carlo (MCMC) statistical method [56], the SA algorithm translates the estimation problem (i.e., estimating the optimum point) into two steps. In the first step, the algorithm generates a new candidate for the next iteration of the Markov chain of the solutions. The second step of the algorithm consists of a stochastic step to evaluate if the new candidate should be accepted or rejected as the next solution of the chain. The SA algorithm iteratively assesses whether or not the transition from the current state of the chain to the new candidate improves the optimization of the objective function.

Here, we explain the implementation of the SA by describing the algorithm's $(k + 1)$ -th iteration. Let $\mathbf{x}^{(k)}$ denote the solution of the objective function obtained from the k -th

iteration of the algorithm. We treat $\mathbf{x}^{(k)}$ current state of the chain and plan to find the next state, that is $\mathbf{x}^{(k+1)}$. Similar to the random walk Metropolis-Hastings method [42, 43, 55], the SA first sample randomly a new candidate \mathbf{x}^* by random perturbation around the current state of the chain by

$$\mathbf{x}^* = \mathbf{x}^{(k)} + \Delta\mathbf{x},$$

where $\Delta\mathbf{x} \sim \mathcal{MVN}(\mathbf{0}, \Sigma)$ represents a small random perturbation sampled from a multivariate normal distribution with mean vector $\mathbf{0}$ and diagonal variance-covariance matrix Σ whose diagonal entries are the variance parameters for coordinate of the input objective function. These variances can be modified per coordinate to take into account the optimization refinement with respect to each coordinate.

The new candidate \mathbf{x}^* is then evaluated through a stochastic accept-reject method to see if \mathbf{x}^* improves the minimum of the objective function or not. Since the objective function $f(\mathbf{x})$ is unknown, the accept reject is applied to the ANN estimate of the objective function $\hat{f}(\mathbf{x}) = \mathcal{F}^L(\mathbf{x}, \hat{\boldsymbol{\theta}}_{opt})$ computed by the method described in section B.1. Since the closed form of the ANN estimate is not available, the improvement of the new candidate \mathbf{x}^* should be evaluated numerically. Hence, the cost difference based on ANN is computed by

$$\Delta\mathcal{F}(\mathbf{x}^*; \mathbf{x}^{(k)}) = \mathcal{F}^L(\mathbf{x}^*, \hat{\boldsymbol{\theta}}_{opt}) - \mathcal{F}^L(\mathbf{x}^{(k)}, \hat{\boldsymbol{\theta}}_{opt}). \quad (\text{B.11})$$

The next step is to accept or reject the new candidate \mathbf{x}^* . The probabilistic accept-reject method is designed to accept always \mathbf{x}^* if it improves the optimization of the objective function [54, 55]. However, if \mathbf{x}^* results in an increase in the cost function, the SA accepts the new state \mathbf{x}^* probabilistically through a Metropolis-Hastings (MH) criterion by

$$P(\text{accepting the transition from } \mathbf{x}^{(k)} \text{ to } \mathbf{x}^*) = \begin{cases} 1, & \text{if } \Delta\mathcal{F}(\mathbf{x}^*; \mathbf{x}^{(k)}) \leq 0, \\ e^{-\Delta\mathcal{F}(\mathbf{x}^*; \mathbf{x}^{(k)})/T_k}, & \text{if } \Delta\mathcal{F}(\mathbf{x}^*; \mathbf{x}^{(k)}) > 0, \end{cases} \quad (\text{B.12})$$

where T_k is the current temperature. This probabilistic acceptance allows the algorithm to escape the local minimum and explore the parameter space to find the minimum point more effectively. If the new candidate is accepted, then $\mathbf{x}^{(k+1)} = \mathbf{x}^*$; however, if the candidate is rejected, the chain remains in the current state, that is, $\mathbf{x}^{(k+1)} = \mathbf{x}^{(k)}$. This MH strategy for searching the minimum in the parameter space is refined iteratively by the cooling schedule [57]. Here, we apply the exponential decay as the cooling scheme:

$$T_{k+1} = \alpha T_k, \quad (\text{B.13})$$

where $0 < \alpha < 1$ is the cooling rate. It is easy to see that in the first iteration of the SA, the high values of the temperature parameter enable the algorithm to explore a wider area of the parameter space to search better for a minimum. If the temperature drops too quickly, the algorithm may not be able to search the entire parameter space and hence may converge to a suboptimal solution. Conversely, if the temperature is cooled too slowly, the algorithm requires many iterations to go from one area to another of the parameter space. Accordingly, the number of iterations increases, and the α rate controls the cooling temperature for balance exploitation and refinement of the minimum in the parameter space. The algorithm is alternated until no significant improvement is observed in the successive iterations or the algorithm reaches a pre-specified maximum number of iterations.

References

- [1] J. Sola, “Cosmological constant and vacuum energy: old and new ideas,” *J. Phys. Conf. Ser.* **453**, 012015 (2013), [arXiv:1306.1527 [gr-qc]].
- [2] J. Sola Peracaula, “The cosmological constant problem and running vacuum in the expanding universe,” *Phil. Trans. Roy. Soc. Lond. A* **380**, 20210182 (2022), [arXiv:2203.13757 [gr-qc]].
- [3] J. Solà Peracaula, À. González-Fuentes and C. Moreno-Pulido, “Towards a unified quantum field theory of dark energy and inflation: unstable de Sitter vacuum and running vacuum,” [arXiv:2601.05218 [gr-qc]].
- [4] I. Y. Park, “Cosmological constant as a finite temperature effect,” *Int. J. Mod. Phys. A* **37**, no. 27, 2250173 (2022), [arXiv:2101.02297 [hep-ph]].
- [5] I. Y. Park, “Quantization of Gravity and Finite Temperature Effects,” *Particles* **4**, no. 4, 468–488 (2021), [arXiv:2109.01647 [hep-th]].
- [6] I. Y. Park, “Finite-temperature renormalization of Standard Model coupled with gravity, and its implications for cosmology,” *Annals Phys.* **481**, 170134 (2025) doi:10.1016/j.aop.2025.170134 [arXiv:2404.07335 [hep-th]].
- [7] J. I. Kapusta and C. Gale, “Finite-Temperature Field Theory: Principles and Applications,” Cambridge University Press (2006).
- [8] M. Le Bellac, “Thermal Field Theory,” Cambridge University Press (2000).
- [9] M. Laine and A. Vuorinen, “Basics of Thermal Field Theory,” *Lect. Notes Phys.* **925**, 1–281 (2016), [arXiv:1701.01554 [hep-ph]].
- [10] C. Moreno-Pulido and J. Sola, “Running vacuum in quantum field theory in curved spacetime: renormalizing ρ_{vac} without $\sim m^4$ terms,” *Eur. Phys. J. C* **80**, no.8, 692 (2020) doi:10.1140/epjc/s10052-020-8238-6 [arXiv:2005.03164 [gr-qc]].
- [11] S. Weinberg, “Cosmology,” Oxford University Press (2008).
- [12] S. Dodelson and F. Schmidt, “Modern Cosmology,” Academic Press (2021).
- [13] C. Balazs, “Observable vacuum energy is finite in expanding space,” [arXiv:2203.16753 [gr-qc]].
- [14] Y. Ageeva, P. Petrov, and M. Shaposhnikov, “Non-renormalizable theories and finite formulation of QFT,” [arXiv:2409.15036 [hep-th]].
- [15] I. Y. Park and P. Y. Wui, “Influence of finite-temperature effects on CMB power spectrum,” [arXiv:2503.07469 [astro-ph.CO]].

- [16] D. Blas, J. Lesgourgues, and T. Tram, "The Cosmic Linear Anisotropy Solving System (CLASS) II: Approximation schemes," *JCAP* **07**, 034 (2011), [arXiv:1104.2933 [astro-ph.CO]].
- [17] CLASS home page: <http://class-code.net/>
- [18] N. Aghanim *et al.* [Planck], "Planck 2018 results. VI. Cosmological parameters," *Astron. Astrophys.* **641**, A6 (2020) [erratum: *Astron. Astrophys.* **652**, C4 (2021)] doi:10.1051/0004-6361/201833910 [arXiv:1807.06209 [astro-ph.CO]].
- [19] S. Agarwal, F. B. Abdalla, H. A. Feldman, O. Lahav and S. A. Thomas, "PkANN - I. Non-linear matter power spectrum interpolation through artificial neural networks," *Mon. Not. Roy. Astron. Soc.* **424**, 1409-1418 (2012) doi:10.1111/j.1365-2966.2012.21326.x [arXiv:1203.1695 [astro-ph.CO]].
- [20] J. d. Olvera, I. Gómez-Vargas and J. A. Vázquez, "Observational Cosmology with Artificial Neural Networks," *Universe* **8**, no.2, 120 (2022) doi:10.3390/universe8020120 [arXiv:2112.12645 [astro-ph.CO]].
- [21] A. T. Chantada, S. J. Landau, P. Protopapas, C. G. Scóccola and C. Garraffo, "Cosmology-informed neural networks to solve the background dynamics of the Universe," *Phys. Rev. D* **107**, no.6, 063523 (2023) doi:10.1103/PhysRevD.107.063523 [arXiv:2205.02945 [astro-ph.CO]].
- [22] S. Pal and R. Saha, "ParamANN: a neural network to estimate cosmological parameters for Λ CDM Universe using Hubble measurements," *Phys. Scripta* **99**, no.11, 115007 (2024) doi:10.1088/1402-4896/ad804d [arXiv:2309.15179 [astro-ph.CO]].
- [23] I. Gómez-Vargas, J. B. Andrade and J. A. Vázquez, "Neural networks optimized by genetic algorithms in cosmology," *Phys. Rev. D* **107**, no.4, 043509 (2023) doi:10.1103/PhysRevD.107.043509 [arXiv:2209.02685 [astro-ph.IM]].
- [24] V. Poulin, T. L. Smith, T. Karwal, and M. Kamionkowski, "Early Dark Energy Can Resolve The Hubble Tension," *Phys. Rev. Lett.* **122**, no. 22, 221301 (2019), doi:10.1103/PhysRevLett.122.221301 [arXiv:1811.04083 [astro-ph.CO]].
- [25] A. G. Riess et al., "A 2.4% Determination of the Local Value of the Hubble Constant," *Astrophys. J.* **826**, no. 1, 56 (2016), [arXiv:1604.01424 [astro-ph.CO]].
- [26] The modified version of CLASS is available at: https://github.com/iparkPSU/modified_CASS_3.2.1_noleak
- [27] J. D. Brown, *Class. Quant. Grav.* **10**, 1579-1606 (1993) doi:10.1088/0264-9381/10/8/017 [arXiv:gr-qc/9304026 [gr-qc]].
- [28] A. J. Nurmagambetov and I. Y. Park, "Quantum-Gravitational Trans-Planckian Radiation by a Rotating Black Hole," *Fortsch. Phys.* **69**, no.10, 2100064 (2021) doi:10.1002/prop.202100064 [arXiv:2007.06070 [hep-th]].

- [29] C. Moreno-Pulido and J. Sola Peracaula, “Renormalizing the vacuum energy in cosmological spacetime: implications for the cosmological constant problem,” *Eur. Phys. J. C* **82**, no.6, 551 (2022) doi:10.1140/epjc/s10052-022-10484-w [arXiv:2201.05827 [gr-qc]].
- [30] C. Moreno-Pulido, J. Sola Peracaula and S. Cheraghchi, “Running vacuum in QFT in FLRW spacetime: the dynamics of $\rho_{\text{vac}}(H)$ from the quantized matter fields,” *Eur. Phys. J. C* **83**, no.7, 637 (2023) doi:10.1140/epjc/s10052-023-11772-9 [arXiv:2301.05205 [gr-qc]].
- [31] P. B. Arnold and O. Espinosa, “The Effective potential and first order phase transitions: Beyond leading-order,” *Phys. Rev. D* **47**, 3546 (1993) [erratum: *Phys. Rev. D* **50**, 6662 (1994)] doi:10.1103/PhysRevD.47.3546 [arXiv:hep-ph/9212235 [hep-ph]].
- [32] B. F. Schutz, “Perfect Fluids in General Relativity: Velocity Potentials and a Variational Principle,” *Phys. Rev. D* **2**, 2762-2773 (1970) doi:10.1103/PhysRevD.2.2762
- [33] B. Carter and I. M. Khalatnikov, “Momentum, vorticity, and helicity in covariant superfluid dynamics,” *Annals Phys.* **219** (1992), 243-265, doi:10.1016/0003-4916(92)90348-P.
- [34] I. Y. Park, ”Hypersurface foliation approach to renormalization of ADM formulation of gravity,” *Eur. Phys. J. C* **75**, no. 9, 459 (2015), [arXiv:1404.5066 [hep-th]].
- [35] I. Y. Park, ”One-loop renormalization of a gravity-scalar system,” *Eur. Phys. J. C* **77**, no. 5, 337 (2017), [arXiv:1606.08384 [hep-th]].
- [36] I. Y. Park, ”Lagrangian constraints and renormalization of 4D gravity,” *JHEP* **04**, 053 (2015), [arXiv:1412.1528 [hep-th]].
- [37] I. Y. Park, ”Holographic quantization of gravity in a black hole background,” *J. Math. Phys.* **57**, no. 2, 022305 (2016), [arXiv:1508.03874 [hep-th]].
- [38] I. Y. Park, ”Revisit of renormalization of Einstein-Maxwell theory at one-loop,” *PTEP* **2021**, no. 1, 013B03 (2021), [arXiv:1807.11595 [hep-th]].
- [39] E. Witten, ”A note on the canonical formalism for gravity,” *Adv. Theor. Math. Phys.* **27**, no. 1, 311–380 (2023), [arXiv:2212.08270 [hep-th]].
- [40] A. Hatefi, E. Hatefi and R. J.Lopez, “Neural networks assisted Metropolis-Hastings for Bayesian estimation of critical exponent on elliptic black hole solution in 4D using quantum perturbation theory,” *JCAP* **09** (2024), 015 [arXiv:2406.04310 [hep-th]].
- [41] E. Hatefi and A. Hatefi, ”Nonlinear statistical spline smoothers for critical spherical black hole solutions in 4-dimension,” *Annals Phys.* **446**, 169112 (2022), [arXiv:2201.00949 [gr-qc]].
- [42] A. Hatefi, E. Hatefi, and R. J. Lopez, ”Modeling the complexity of elliptic black hole solution in 4D using Hamiltonian Monte Carlo with stacked neural networks,” *JHEP* **10**, 034 (2023), [arXiv:2307.14515 [gr-qc]].

- [43] A. Hatefi and E. Hatefi, “Sequential Monte Carlo with cross-validated neural networks for complexity of hyperbolic black hole solutions in 4D,” *Eur. Phys. J. C* **83** (2023) no.11, 1083 [arXiv:2308.07907 [hep-th]].
- [44] J. Solà Peracaula, A. Gómez-Valent, J. de Cruz Perez and C. Moreno-Pulido, “Running vacuum against the H_0 and σ_8 tensions,” *EPL* **134**, no.1, 19001 (2021) doi:10.1209/0295-5075/134/19001 [arXiv:2102.12758 [astro-ph.CO]].
- [45] Armin Hatefi, Ehsan Hatefi, and I. Y. Park, work in progress.
- [46] LeCun, Y., Bengio, Y., & Hinton, G. (2015). ”Deep learning,” *Nature*, *521*(7553), 436–444.
- [47] Hastie, T., Tibshirani, R., & Friedman, J. (2009). *The Elements of Statistical Learning: Data Mining, Inference, and Prediction*, Springer-Verlag, New York.
- [48] Goodfellow, I., Bengio, Y., & Courville, A. “Deep learning”, MIT press. (2016)
- [49] Rumelhart, D. E., Hinton, G. E., & Williams, R. J. (1986). ”Learning representations by back-propagating errors,” *Nature*, *323*(6088), 533-536.
- [50] Prince, Simon JD. Understanding deep learning. MIT Press, 2023.
- [51] J. Nocedal and S. J. Wright, *Numerical Optimization*. New York, NY, USA: Springer, 2006.
- [52] N. M. Nawi, M. R. Ransing, and R. S. Ransing, ”An improved learning algorithm based on the Broyden-Fletcher-Goldfarb-Shanno (BFGS) method for back propagation neural networks,” in *Sixth International Conference on Intelligent Systems Design and Applications*, 2006, vol. 1, pp. 152–157.
- [53] G. James, D. Witten, T. Hastie, and R. Tibshirani, *An Introduction to Statistical Learning*. New York, NY, USA: Springer, 2013.
- [54] D. Bertsimas and J. Tsitsiklis, ”Simulated annealing,” *Statistical Science*, vol. 8, no. 1, pp. 10–15, 1993.
- [55] C. P. Robert and G. Casella, *Monte Carlo Statistical Methods*, vol. 2. New York, NY, USA: Springer, 1999.
- [56] C. Andrieu, N. De Freitas, A. Doucet, and M. I. Jordan, ”An introduction to MCMC for machine learning,” *Machine Learning*, vol. 50, no. 1, pp. 5–43, 2003.
- [57] Y. Xiang, S. Gubian, B. Suomela, and J. Hoeng, ”Generalized simulated annealing for global optimization: The GenSA package,” *Journal of Statistical Software*, vol. 54, no. 3, pp. 1–13, 2013.